

Analysis of two-dimensional microdischarge distribution in dielectric-barrier discharges

A Chirokov¹, A Gutsol¹, A Fridman¹, K D Sieber², J M Grace²
and K S Robinson²

¹ Department of Mechanical Engineering, Drexel University, Philadelphia, PA, USA

² Eastman Kodak Company, Rochester, NY, USA

E-mail: chirokov@drexel.edu

Received 2 April 2004

Published 5 October 2004

Online at stacks.iop.org/PSST/13/623

doi:10.1088/0963-0252/13/4/011

Abstract

The two-dimensional spatial distribution of microdischarges in atmospheric pressure dielectric-barrier discharges (DBDs) in air was studied.

Experimental images of DBDs (Lichtenberg figures) were obtained using photostimulable phosphors. The storage phosphor imaging method takes advantage of the linear response of the phosphor for characterization of microdischarge intensity and position. A microdischarge interaction model in DBDs is proposed and a Monte Carlo simulation of microdischarge interactions in the discharge is presented. Comparison of modelled and experimental images indicates interactions and short-range structuring of microdischarge channels.

1. Introduction

Dielectric-barrier discharges (DBDs), or silent discharges, have a number of industrial applications. For example, in addition to ozone generation, the DBD in air is commonly used in the web conversion industry, where it is known commercially as ‘corona discharge treatment’. It is used to treat polymer surfaces in order to promote wettability, printability and adhesion [1, 2]. This non-equilibrium discharge is especially advantageous for the web conversion industry because it operates at atmospheric pressure and ambient temperature. The use of the so-called corona treatment, as well as other various surface modification methods for the manufacture of many different types of products on moving webs, is extensively described in the literature.

Recently there has been interest in characterizing and understanding the diversity of phenomena that can be found in atmospheric pressure discharges [3]. The nature of the discharge depends on the gas mixture employed, the dielectric and the operating conditions. Both diffuse and filamentary discharges are observed at atmospheric pressure and the experimental conditions leading to ordering or patterning of barrier discharges have been reported [3]. The development of experimental methods, such as imaging techniques,

for quantitative characterization of microdischarges and associated cooperative phenomena in atmospheric pressure discharges is lacking. Furthermore, theoretical models describing cooperative phenomena in these discharges are not complete.

In this paper, we report an experimental technique that employs the inherent linearity of photostimulable phosphors for quantitative imaging of microdischarges as well as a novel theoretical model describing microdischarge interactions and cooperative phenomena in the barrier discharges. Experimental and simulated images were compared using two approaches: Voronoi polyhedra and the radial correlation function. Microdischarge interactions leading to short-range structuring of microdischarge channels are found.

2. The physical nature of microdischarge interaction and structuring

In most cases, DBDs are not uniform and consist of numerous microdischarges distributed in the discharge gap as can be seen in figures 1 and 2. The physics of microdischarges is based on an understanding of the formation and propagation of streamers, and consequent plasma channel degradation.

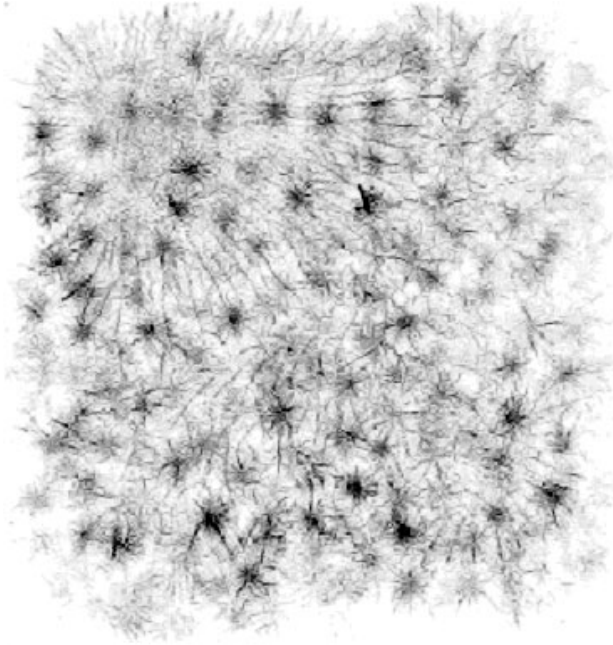


Figure 1. Storage phosphor image of filaments in a DBD gap in air obtained from an experimental set-up using one applied excitation cycle at 20.4 kHz and a discharge gap of 4.57 mm.

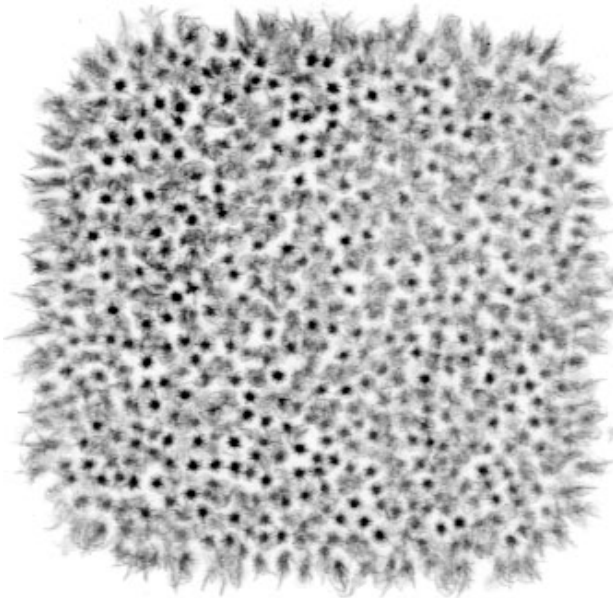


Figure 2. Storage phosphor image of filaments in a DBD gap in air obtained from an experimental set-up using ten excitation cycles at 20.9 kHz and a discharge gap of 0.762 mm.

Streamers are local ionization waves usually moving from anode to cathode to meet avalanches propagating in opposite directions. Streamers move very fast (about 10^8 cm s^{-1}) and cover the distance between electrodes in nanoseconds. The electrons in the conducting plasma channel established by the streamers dissipate from the gap in about 40 ns, while the heavy and slowly drifting ions remain in the discharge gap for several microseconds (table 1). Deposition of electrons from the conducting channel onto the anode dielectric barrier results in charge accumulation and prevents new avalanches

Table 1. Calculated microdischarge characteristics for the experimental system used in this study (with discharge gap 1 mm).

| | Duration time | Charge transferred (C) |
|--------------------------------|---------------|------------------------|
| Microdischarge (0.2 mm radius) | 40 ns | 10^{-9} |
| • Electron avalanche | 10 ns | 10^{-11} |
| • Cathode-directed streamer | 1 ns | 10^{-10} |
| • Plasma channel | 30 ns | 10^{-9} |
| Microdischarge remnant | 1 ms | $\geq 10^{-9}$ |

and streamers nearby until the cathode and anode are reversed (if the applied voltage is not much higher than the voltage necessary for breakdown). The operating frequency of the discharges used here is around 20 kHz, and therefore the voltage polarity reversal occurs within $25 \mu\text{s}$. After the voltage polarity reverses, the deposited negative charge facilitates the formation of new avalanches and streamers in the same spot. As a result, a many-generation family of streamers is formed that is macroscopically observed as a bright filament that appears to be spatially localized. It is important to clarify and to distinguish the terms avalanche, streamer and microdischarge. An initial electron starting from some point in the discharge gap (or from the cathode or the dielectric that covers the cathode in the case of a well developed DBD) produces secondary electrons by direct ionization and develops an electron *avalanche*. If the avalanche is big enough (Meek condition [28]) then a cathode-directed streamer is initiated (usually from the anode region). A *streamer* is a very fast ionization wave that bridges the gap in a few nanoseconds and forms a conducting *channel* of weakly ionized plasma [29, 30]. An intense electron current will flow through this plasma channel until the local electric field collapses. Collapse of the local electric field is caused by the charges accumulated on the dielectric surface and ionic space charge (ions are too slow to leave the gap for the duration of this current peak). The group of local processes in the discharge gap initiated by the avalanche and developing until electron current termination is usually called a *microdischarge*. After electron current termination there is no more electron-ion plasma in the main part of the microdischarge channel, but a high level of vibrational and electronic excitation in the channel volume, along with charges deposited on the surface and ionic charges in the volume, allows us to separate this region from the rest of the volume and we call it a microdischarge *remnant*. Positive ions (or positive and negative ions in the case of an electronegative gas) of the remnant slowly move to the electrodes, resulting in a low and very long ($\sim 10 \mu\text{s}$ for 1 mm gap) falling ion current. A microdischarge remnant will facilitate formation of a new microdischarge in the same spot when the polarity of the applied voltage changes. That is why it is possible to see single *filaments* in DBD. If microdischarges formed at a new spot each time the polarity changed, the discharge would appear uniform. Thus the *filaments* in a DBD is a group of microdischarges that form at the same spot each time the polarity is changed. The fact that a microdischarge remnant is not fully dissipated before the formation of the next microdischarge is called the memory effect [21, 25].

The charge distribution associated with streamers and the local electric field in the gap associated with the plasma channel

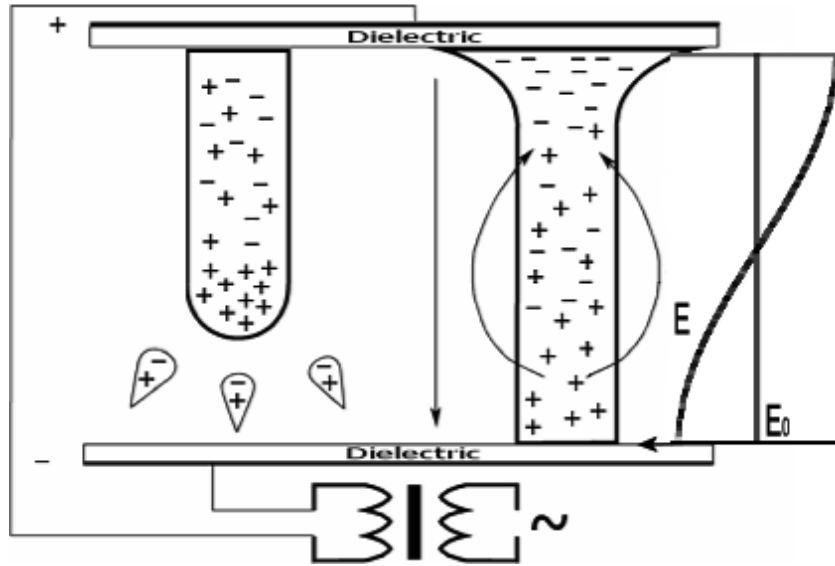


Figure 3. Streamer formation (left-hand side) plasma channel (and microdischarge remnant) and electric field distortion (right-hand side) are due to space charges. The solid curve is the superposition of the electric field from the microdischarge and the applied electric field; the dashed line is the applied electric field. In the presence of a positive space charge, the electric field is increased at the cathode and decreased at the anode.

and the microdischarge remnant is shown in figure 3. The left-hand side of figure 3 shows a streamer propagating from the anode to the cathode while attracting additional avalanches. The resulting plasma channel and the microdischarge remnant that forms, shown on the right-hand side of the figure, have a net positive charge because the electrons leave the gap much faster than the ions. The residual positive charge (together with the deposited negative charge in the case of a dielectric surface) influences the formation of nearby families of avalanches and streamers and, therefore, the formation of neighbouring microdischarges. The mechanism of influence is the following: the positive charge (or dipole field in the case of deposited negative charge) intensifies the electric field in the cathode area of the neighbouring microdischarge and decreases the electric field in the anode area. Since the avalanche-to-streamer transition depends mostly on the near-anode electric field (from which new streamers originate), the formation of neighbouring microdischarges is actually prevented, and the microdischarges effectively repel each other. The quasi-repulsion between the microdischarges leads to formation of short-range order that is related to a characteristic repulsion distance between microdischarges. Observation of this cooperative phenomenon depends on several factors, including the number of microdischarges occurring and the operating frequency. For example, when the number of microdischarges is not large enough (when the average distance between the microdischarges is larger than the characteristic interaction radius), no significant microdischarge interaction is observed. When the ac frequency is too low to keep the microdischarge remnants from dissipating (a low frequency means that the period is longer than the typical lifetime of a microdischarge remnant or the ‘memory effect’ lifetime, which is estimated to be 1 ms for our system), microdischarge repulsion effects are not observed. In addition, DBD cells operated at very high frequencies in the megahertz region will not exhibit microdischarge repulsion because the very

high frequency switching of the voltage interferes with ions still moving to the electrodes (for a detailed explanation of ion trapping effect and estimation of frequency at which it becomes significant see [31]). Our observations of cooperative phenomena between microdischarges will be discussed below from both an experimental and a theoretical perspective.

3. Experimental set-up and results

The parallel plate configuration of the dielectric barrier cell used in this study is shown in figure 4. The cell consists of an aluminium chamber equipped with a high voltage electrode assembly and a gas-tight Plexiglas® lid. The bottom of the $33 \times 33 \times 7.6 \text{ cm}^3$ aluminium chamber was covered with a $30.5 \times 30.5 \times 0.1 \text{ cm}^3$ high purity quartz dielectric barrier. The dielectric-covered bottom of the chamber served as the ground electrode. The high-voltage electrode assembly was located inside the aluminium chamber and a high-voltage electrical feedthrough in the Plexiglas lid was used to bring power into the chamber. The Plexiglas lid also contained a ultraviolet (UV)-grade high-purity quartz optical window. The gas inlet and outlet ports were located on the aluminium chamber at ground potential. To ensure gas purity and humidity control in our equipment, a 1/3 PSI ‘popet’ type check valve was installed on the gas outlet. The use of the check valve allows a small amount of positive pressure to build up inside the cell, thereby minimizing gas diffusion into the cell from the outside. The high voltage electrode was held in a Delrin® polymer assembly and a low-resistance connection between the conducting surface of the high-voltage electrode and the high-voltage lead was accomplished by means of a spring-loaded electrical contact with the aid of an indium-gallium alloy to wet the conducting surfaces. The high-voltage electrode used in this study was a $5 \times 5 \text{ cm}^2$ area of low-resistivity indium tin oxide (ITO) coated on a 1 mm thick

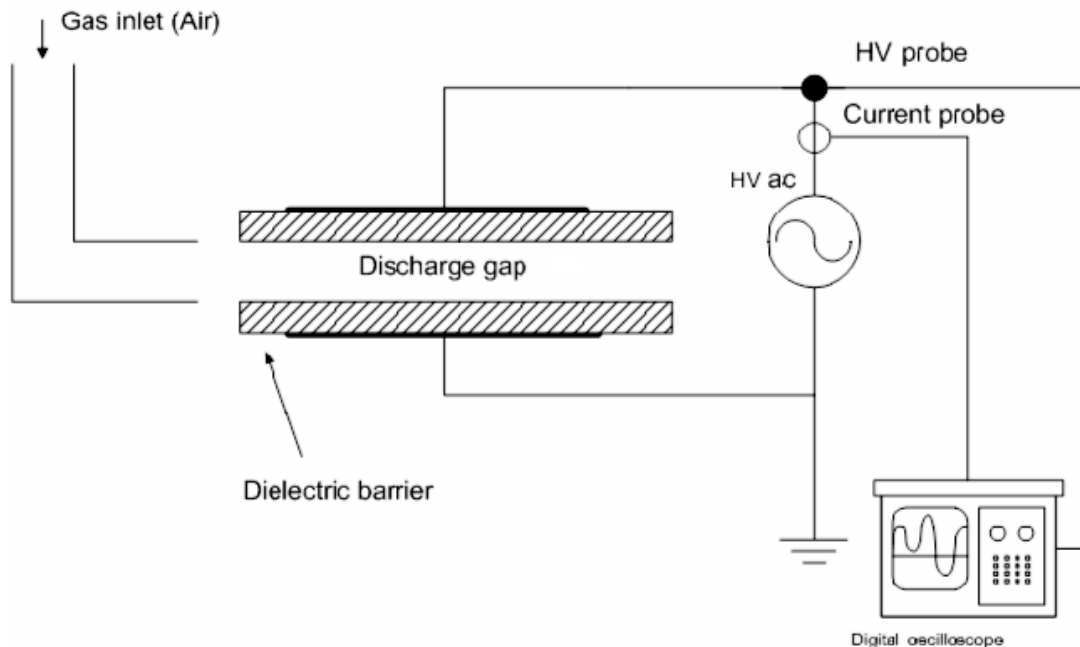


Figure 4. A schematic of the experimental set-up showing the barrier discharge cell with two quartz dielectrics.

high-purity quartz substrate. This optically transparent high-voltage electrode was mounted in the cell so that the insulating quartz surface of the electrode was facing the discharge gap. The distance between the surfaces facing the discharge gap (also referred to as the electrode gap) in the cell could be varied between 4.57 and 0.762 mm. The electrode gap setting normally used was 1.52 mm. This gap setting is typical of that used in DBDs in commercially available web-converting equipment.

The gas flow through the cell was controlled using mass flow controllers (Tylan RO-18 electronics with appropriate controllers). Typical flow rates were around 1 slpm (standard litre per minute). All studies reported here were performed in ambient air at room temperature. The air to the system was supplied by a laboratory compressor and was filtered and dried before use. The water content of the air was measured on-line using a calibrated Luft infrared analyser (MSA LIRA) and was determined to be less than 0.3% H₂O by volume.

The nominal operating frequency for most of the experiments was approximately 20 kHz. This frequency is typical of the frequencies employed in commercially available power supplies found on web-conversion equipment. A Tektronix P6015A high-voltage probe and a Pearson current transformer (model 2100) were installed on the high-voltage side of the step-up transformer. The voltage and current waveforms from the set-up were acquired using a high-speed digital oscilloscope (Tektronix 544A) and the dissipated power was calculated from the waveforms using either the math functions in the digital oscilloscope or by analysing the current and voltage waveforms directly by the Lissajous method [4, 5]. Typical steady-state power settings employed in the cell and measured on the high-voltage (secondary) side of the transformer were between 20 and 150 W.

Both the voltage amplitude and voltage pulse train duration were used to control the exposure of the imaging plate (described below) to the discharge. This was accomplished

by the use of two waveform generators. The high-frequency waveform provided by a Wavetek model 29 programmable digital waveform generator was gated by an HP-8111A waveform generator to apply the desired gated waveform to the cell. An ENI model 1140LA power amplifier amplified the gated driving waveform. The output of the power amplifier was stepped up to a high voltage using a matching network and a commercially available power transformer (Plasma Technics, Racine, WI) and applied to the high-voltage electrode of the DBD cell. The load-matching technique employed allowed the cell to be operated in a frequency window between 10 and 25 kHz. The waveform traces observed in our system show evidence of transformer ringing, and the circuit resonance appears to limit the lowest achievable time-integrated dissipated (secondary) power. When appropriate, the time-integrated power per unit area dissipated on the imaging plate was used as a metric for comparing images during this study.

The emission spectrum of the discharge was acquired with a grating monochromator using a PAR model 1460 OMA console with a model 1420 intensified diode array detector. The equipment was wavelength and intensity calibrated before use. All spectra were background subtracted and intensity corrected. Further optical characterization of the discharge was accomplished by monitoring the time-resolved emission of the discharges using the N₂ 380 nm emission line. The optical emission from the discharge was acquired using a fibre optic, passed through a high-throughput monochromator and detected by a photomultiplier tube (PMT) (Hamamatsu R928). The time resolution of the PMT and electronics in our measuring system was approximately 1–2 ns. We chose to monitor the 380 nm emission from the C³Π_u level of N₂ for convenience and because the emission lifetime is of the order of 40 ns [6]. The duration of the current pulse responsible for the formation of molecular-excited states by electron impact processes in a typical microdischarge is of the

order of 10–40 ns [7]. The lifetime of the molecular nitrogen emission from the $C^3\Pi_u$ system is short in comparison with the current pulse duration, and therefore light pulses from individual microdischarges can be detected using the type of set-up described above. The optical signal from the PMT was digitized using a high-speed digital oscilloscope (Tektronix 544(a)) for further analysis. Optical emission was acquired either from the side of the discharge or in the direction perpendicular to the plane of the discharge through the ITO high-voltage electrode. Counting of optical pulses from the discharge was done with the fibre optic, viewing the discharge through the high-voltage electrode.

The Health Imaging Division of the Eastman Kodak Company provided the storage phosphor imaging plates used in this study. The imaging plates were identical to commercially available SO-240 general-purpose radiography screens, except that the plates were fabricated without a protective overcoat³. This was done to increase the sensitivity of the imaging plate for imaging microdischarges. In our investigations, the imaging plate was always placed on a dielectric-covered ground-electrode surface. It should be noted that the use of storage phosphor plates requires some care concerning exposure to ambient light. Many fluorescent lamps can expose the plate and cause a background fogging of the plate. A plastic filter over the plate will allow room light handling without causing background on the plate; however, during and after an exposure the plate should be kept in the dark to avoid erasing the photostimulable centres formed in the phosphor. The erasure characteristics of these plates can be found in the literature. The imaging plates were read out using a commercially available storage phosphor reader (Molecular Dynamics Phosphor Imager Model 425 with Molecular Dynamics Image Quant software). The pixel size setting for the phosphor reader was $88 \times 88 \mu\text{m}^2$ and the PMT voltage was the default scanner setting of 800 V. The background noise of an erased, unexposed plate was below 5 counts per pixel. The background noise of the imaging plate could be virtually eliminated by proper setting of the lower discriminator level in the Image Quant software. The signal from the exposed plate during scanning was low due to the extremely small amount of energy deposited during some of the experiments; however, proper setting of the lower level discrimination and adjustment of the linear grey scale range allowed easy visualization of the image. Pixel counts in a typical image feature attributed to a single microdischarge were a minimum of 400 times greater than the background noise. Eight-bit (8-bit) and 14-bit TIFF files were generated from the scanner for further image analysis using either commercially available or custom-written image-analysis programs.

A typical microdischarge imaging experiment starts with erasing an imaging plate and setting up the cell. The discharge cell is set-up by installing the imaging plate on the ground-electrode dielectric in the appropriate location in the cell and setting the distance between the imaging plate and the dielectric-covered bottom of the high-voltage electrode to the desired setting. After setting the discharge gap, the discharge cell is closed and the gas flow started. The cell is purged until the desired humidity is obtained (0.3%). The lights in

the room are turned off and the imaging plate is exposed to the discharge. The secondary voltage and current waveforms are synchronously acquired during the discharge exposure. In many cases, synchronous optical pulse measurements are acquired as well. After the imaging plate is exposed to the discharge, the cell is allowed to purge to remove ozone and oxides of nitrogen, and then the plate is removed and read out with a storage phosphor reader. After reading, the plate is erased and placed back into the cell for the next experiment.

4. Imaging of microdischarges

Various techniques for imaging microdischarges have been described in the literature. One of the oldest methods for imaging microdischarges is the Lichtenberg method [8, 9]. The photographic images generated by this technique are known as Lichtenberg figures, although the original Lichtenberg figures were produced in a different way [8]. In the photographic method, the light emitted from a microdischarge is imaged using a piece of photographic film. The film may be placed underneath a transparent insulator, such as glass or quartz, to record the plasma optical emission, or it may be exposed directly to the discharge. The information obtained from such images includes the physical dimension of the footprint of the microdischarge, as well as an estimate about the microdischarge density in terms of strikes-per-unit area. Images of electrostatic phenomena, regardless of how they are generated, are generally referred to as Lichtenberg figures. The work reported here demonstrates the use of imaging plates containing photostimulable phosphor for characterization of DBDs in air through the use of Lichtenberg-type figures.

Photostimulable phosphors are also known as ‘storage’ phosphors. This unique class of inorganic materials has the remarkable property of ‘storing’ the energy from ionizing radiation in the form of radiation-induced lattice defects whose energy can be liberated by selective photostimulation. The particular material used in this study is the same storage phosphor used for computed radiography applications—europium-activated barium fluorobromide. This phosphor crystallizes with the Matlockite structure and has the chemical composition $\text{BaFBr}_{1-x}\text{I}_x : \text{Eu}$ (BFBI). BFBI has been studied extensively and optimized for the creation of point defects like F centres upon exposure to x-radiation. The number of defects created is proportional to the energy exposure or dose. The phosphor is called ‘photostimulable’ because the radiation-induced defects can be ‘read out’ by stimulating the defects with light (photostimulation). In the case of BFBI, irradiation into the F centre absorption band with a He–Ne laser promotes defect-recombination processes that lead to energy transfer to the Eu^{+2} activator cation, resulting in the characteristic blue Eu^{+2} emission. Raster scanning of the exposed imaging plate allows the two-dimensional energy pattern on the plate to be digitized. The plate can be ‘erased’ or cleaned of photostimulable residuals after reading by flooding the exposed surface with light of the appropriate energy. It is then available for reuse.

Storage phosphors have been applied to a variety of imaging problems. For example, the use of photostimulable storage phosphor plates in radiography is well known and the technique is commonly referred to as computed radiography.

³ The authors thank and acknowledge Mr David Steklenski of Kodak Health Imaging for providing the imaging plates used in this study.

Photostimulable phosphor systems are used for imaging synchrotron radiation [10], as well as for neutron detection in neutron diffraction and neutron radiography [11]. Storage phosphor imaging is reported for detection of both soft x-rays and vacuum UV radiation from synchrotrons and lasers [12]. Biochemical applications of storage phosphor imaging include the imaging of electrophoretic gels containing radionuclides (including ^{32}P , ^{14}C and ^{35}S) for DNA characterization studies [13]. The use of storage phosphors to image electron beams in transmission electron microscopy and for electron beam dosimetry has been reported [14]. Storage phosphor screens in combination with beta radiation have been used to image paper in manufacturing processes [15]. We describe here what we believe is the first reported use of storage phosphor imaging plates for microdischarge imaging.

The use of storage phosphor imaging plates offers some advantage over photographic film for imaging microdischarges in barrier discharges. For example, in contrast to the nonlinear sensitometric response of photographic emulsions, storage phosphor plates show a wide-range linear response with respect to impinging energy. This means that the signal intensity at any particular pixel is directly proportional to the amount of energy deposited. We have verified in our equipment that the signal intensity in the images is linearly proportional to the dissipated energy in the barrier discharge cell.

The resolution of a storage phosphor imaging system is limited by the resolution of the imaging plate. The typical resolution of the general purpose imaging plates for x-ray imaging is between 3 and 4 line pairs per millimetre. The resolution of these imaging plates with respect to low-energy electron bombardment is not known. In practice the typical pixel size employed in the scanners lies between 80×80 and $170 \times 170 \mu\text{m}^2$. Although it can be argued that storage phosphor plates are not as high in resolution as photographic film, the spatial resolution is sufficient to allow imaging of microdischarges. It is known in the literature that the value of the radius of a single microdischarge from a barrier discharge is of the order of $100 \mu\text{m}$ [16]. Our investigations suggest that lower resolution images with larger pixel sizes ($176 \times 176 \mu\text{m}^2$ pixel size) are adequate for characterizing the microdischarge spatial distributions. At higher resolution scanner conditions, we believe that the storage phosphor method has sufficient sensitivity to be capable of imaging single microdischarges. A major advantage of this method is the ease with which digital data files can be generated for further examination with image analysis methods.

The minimum energy for creation of a photostimulable site in the BFBI lattice is determined by the optical absorption edge of the material because the generation of excitons leading to the formation of photostimulable centres is quite efficient near the optical-absorption band edge in these materials. Reflectance measurements of BFBI screens, shown in figure 5, show decreasing optical absorption at wavelengths longer than 300 nm (approximately 4 eV). The optical-absorption edge measured for the screen is not as pronounced as that of the pure phosphor because of additional optical absorptions attributed to proprietary additives in the screen. For comparison, the optical emission spectra of the atmospheric pressure DBDs investigated in this study are given in the same figure. The discharges show most of their emission at wavelengths between

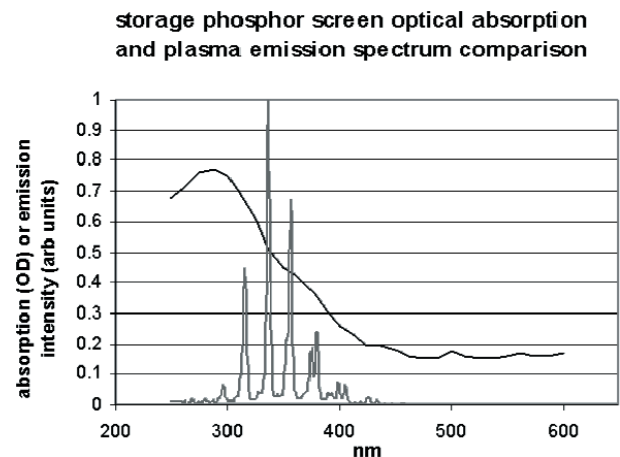


Figure 5. A comparison of the optical emission spectrum (peaks at the bottom) from the DBD cell with the optical absorption spectrum of the storage phosphor imaging plate used in these studies.

300 and 450 nm. Although we have not shown the results here, the discharges also have negligible emission intensity between 500 and 800 nm. This is an important observation because the stimulation region for the barium fluorohalide photostimulable phosphor (attributed to F centre optical absorption) is located in this spectral window. Significant emission from the discharge in this region would have some effect on the observed sensitivity of the imaging system. The lack of optical emission from the discharge in the region of F centre absorption suggests that there is little, if any, signal intensity erasure during plate exposure to the discharge. There was no evidence of signal saturation during our investigations; however, we did not extend our work to extremely high power levels. We have not investigated, in any depth, the stability of pre-existing photostimulable centres in the imaging plate with respect to the extremely large high-frequency voltages employed in barrier discharges, but the linearity of the signal response with respect to discharge exposure suggests that this effect is not significant.

Storage phosphor imaging plates can be excited both optically and by electron bombardment. It is important to assess the relative contribution of each type of excitation in the imaging system. The data given in figure 5 indicate that there is some optical charging of the storage phosphor plate when the plate is exposed to a barrier discharge in air because of the overlap between the optical emission from the plasma and the optical absorption of the storage phosphor. To determine the contribution of photostimulable centres from the discharge UV emission to the overall image intensity, we ran a set of experiments where the position of the imaging plate with respect to the quartz dielectric barrier was changed. In one set of exposures, the imaging plate was placed above the quartz dielectric and directly exposed to the discharge. A second set of exposures was done where the imaging plate was located under the quartz dielectric so that only light emitted from the discharge could cause a signal on the imaging plate. The dissipated power, the exposure time, the electrode gap and the percentage of water in the atmosphere were held constant during these experiments. Note that the capacitance of the cell was not changed by switching the positions of the dielectric with respect to the imaging plate and, therefore, any observed changes in the resulting image must be related to differences

in the excitation of the imaging plate. Instead of a slight drop in the overall intensity of the image, as would be expected if the photostimulated luminescence was attributable mostly to optical excitation, we found that the overall intensity of the signal readout from the imaging plate (when it was located under the dielectric during exposure) was about an order of magnitude lower than the signal obtained during readout when the plate was exposed directly to the discharge. We interpret these observations to mean that the formation of photostimulable centres as a result of UV excitation comprises about 10% of the total signal intensity in the image. We conclude that electron bombardment of the phosphor from the microdischarge is the main excitation responsible for the formation of photostimulable centres on the imaging plate [17]. The following section presents examples of microdischarge images obtained by the storage phosphor method.

5. Experimental storage phosphor images of microdischarges

Figure 1 shows an 8-bit image of a DBD in air obtained from the experimental set-up. In this experiment, the flow rate of air was 5 slpm and the gap was 5 mm. The real discharge area was $5 \times 5 \text{ cm}^2$. The discharge image presented in figure 1 was obtained using one applied excitation cycle at 20.4 kHz. Digital oscilloscope traces from the secondary side of the transformer indicate that the high-voltage transformer shows some ringing after the initial amplified waveform is applied to the primary side. An examination of synchronous-optical pulse counting from the discharge showed that the discharge actually occurred over 1.5 voltage cycles. The microdischarge features in figure 1 appear to be randomly distributed.

Changing the discharge conditions, such as the gap setting or the driving voltage frequency and amplitude, can result in significantly different microdischarge images. An example of this is shown in figure 2. Figure 2 was obtained using discharge conditions of ten applied cycles at 20.9 kHz with an airflow rate of 1 slpm and a gap of 0.762 mm. Images taken under these same conditions with applied voltage cycles more than five were all quite similar, except that the image intensity increases linearly with increasing discharge exposure time. Note that the images do not show localization of microdischarge density around the edges of the electrode. This indicates that electric field localization at the electrode edges is not a strong effect under these experimental conditions. The sharp, black points correspond to microdischarges that are stationary and occur repeatedly in the same location. We observe that the microdischarges become stationary in our apparatus under these conditions at between five and ten cycles of applied voltage. Microdischarges, or families of streamers, are the main vehicles of plasma-chemical processes in DBDs, and the localization of the microdischarge position is undesirable. From the practical perspective of web treatment, localization can lead to spatially non-uniform surface modification.

6. Microdischarge interaction model and simulation results

To model the phenomena observed in the experimental images, we begin by describing the formation of a microdischarge in

the DBD. The general microdischarge description is based on consideration of the formation and propagation of avalanches and streamers. The simplest set of equations containing the basic physics necessary to describe the microdischarge was used in the simulations [18–20, 27]. The microdischarge description used here takes into account gas composition, pressure, power and current and gives the main characteristics of the different microdischarge stages. The modelled microdischarge characteristics are given in table 1.

The experimental images shown in figures 1 and 2 suggest that filaments (microdischarge families) space themselves out. To model the interaction between microdischarges, we consider that the avalanche-to-streamer transition depends only on the local value of the electric field and the discharge gap. Once the microdischarge is formed, the electric field of the microdischarge remnant decreases the external applied electric field in the fashion described above. The electric field distortion around the microdischarge remnant, as calculated by Poisson's equation, is shown on the right-hand side of figure 3. The average effective field in the local region near the anode where the avalanche-to-streamer transition occurs decreases and, as a consequence, the formation of new streamers at the same location is prevented unless there is an increase in the external applied voltage. We should emphasize that observation of microdischarge filaments in a DBD is possible when both electrodes are covered by the dielectric as well as in the case where one electrode is not covered, meaning that no surface discharge can be deposited on this electrode. In the case of a metal electrode, the volume charges induce formation of the image charge on the electrode surface. So with both metal and dielectric surfaces, an electrical 'dipole' is formed by positive volume and negative surface charges. When the externally applied field varies quickly with respect to the microdischarge remnant dissipation lifetime in the system, the microdischarges will stay separated by a distance corresponding to the length scale of the field inhomogeneity. If the applied electric field is high enough, it will cause microdischarges to develop in all the unoccupied spaces, so that the gap becomes filled from end to end.

We consider two types of applied voltage in our analysis of the DBD: a unipolar voltage and an alternating voltage. In the unipolar or dc case (before polarity changes), one of the electrodes remains positive and the other is negative. The streamer always moves in one direction, so that subsequent streamers and thus microdischarges have a small probability of forming in the same place until the microdischarge remnant has dispersed. A different situation appears in the case of the alternating voltage. There is no need to wait until the microdischarge remnant dissipates. Instead, the probability of appearance of a streamer in the location of the microdischarge remnant increases when the voltage is switched. After the voltage is switched, the electric field of the microdischarge remnant adds to the strength of the applied electric field, thereby increasing the local field. The increased electric field increases the likelihood for a new streamer to occur at the same place. The net result is that if the original streamer forms just before voltage switching, there is an increased probability of streamers occurring in the same place or immediate vicinity. The next section presents the Monte Carlo approach we use to simulate microdischarge interactions. We do not consider

avalanches that are not powerful enough to initiate streamers as the electrical charge transferred by an individual avalanche is much smaller than the charge transferred by a microdischarge.

A probability-driven cellular automata (CA) scheme was used in our modelling approach [22]. The general CA scheme consists of a lattice of cells that can have any dimension and size coupled with a set of rules for determining the state of the cells. At any time, a cell can be in only one state. We used a two-dimensional stochastic CA scheme. From a physical perspective, each cell represents a volume in the gap located between the electrode surfaces. The upper and lower surfaces of each cell are bounded by the dielectric surfaces of the electrodes themselves, and the height of each cell is defined by the gap distance. We define $M_{i,j}$ as a matrix of states of the CA that can change with time. The value of the time step in the simulation is important and is defined by the variable dt . The cell transformation rules in our simulation take into account not only the initial state of the cell but the state of neighbouring cells and some external information as well. Therefore, we used the extended form of CA in which some data about real physical values (e.g. charge density, electric field, energy release, random fluctuations) are kept in each cell in addition to the information about the discrete state of the cell. The CA transformation rules define a new state for a cell after a given time step, using data about the states of all the cells in the CA and additional information, such as the driving voltages imposed upon the system as a whole. It is assumed that the probability for the occurrence of the streamer depends only on the local value of the electric field. The position of a streamer strike is determined using a Monte Carlo decision for given probability values in each cell. Once the position of streamer strike is known, a plasma channel is formed at the same place and the total charge transferred by this microdischarge is assigned to the cell to be used later in electric field calculations. Since streamers can appear randomly in time as well as in space, an additional Monte Carlo simulation was used to decide whether a streamer will occur or not. If the streamer will not strike, the plasma channel will not form and there will be no microdischarge. Figure 6 shows the flow chart for this procedure.

The simulation code was developed to work with voltage waveforms of arbitrary shape. The input parameters to the program are the simulation time (e.g. number of cycles at a given frequency for the case of the ac voltage), the driving voltage waveform (sinusoidal, square, triangular), the size of the CA (simulation lattice size) and the geometry of the discharge gap. The charge transferred by the microdischarge is not specified as an input parameter. Instead it is dynamically calculated during simulation based on the local electric field strength. The charge transferred by an individual microdischarge decreases the electric field inside the microdischarge channel because it creates a local electric field opposing the externally applied electric field (collapse of the electric field in the microdischarge channel). We assume that the total charge transferred by the microdischarge is the amount of charge that decreases the local electric field to zero (in other words, charge passes through the microdischarge channel established in a CA cell until the local electric field drops to zero). This assumption that the charge transferred by the microdischarge collapses the electric field to zero appears to adequately represent the

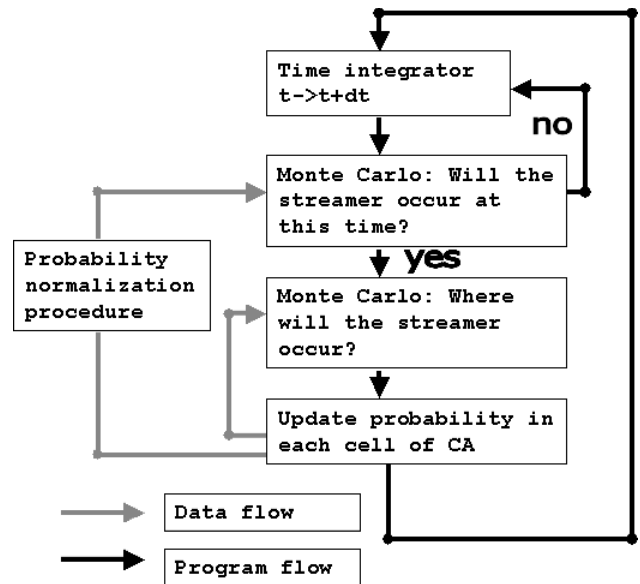


Figure 6. Flow chart for the space and time coupled Monte Carlo simulation.

interaction between microdischarges, although it seems not to be generally true, especially in the case of electronegative gases. The simulation model also uses the charge transfer information to calculate the theoretical current waveform from the discharge for a given input voltage waveform.

The probability of a streamer striking is calculated from the local electric field using the following formula,

$$P(E) = 1 - \frac{1}{1 + \exp(S((E - E_0)/E_0))}, \quad (1)$$

where E is the electric field in the cell, E_0 is the critical electric field necessary for streamer formation given by the Meek condition [28] and S is a parameter related to the ability of the discharge to accumulate memory, about previous microdischarges. For a further discussion of the memory effect in DBDs, see [25]. When S is large, the memory effect has a negligible influence on the operation of DBDs, and the probability function will be a step function that represents Meek's condition for streamer formation. When S is small, the memory effect significantly affects the probability of streamer formation. It is known that streamer formation is influenced by a number of factors. The presence of the vibrationally and electronically excited species and negative ions increases the ionization coefficient (first Townsend coefficient) and thus a lower electric field is required for the avalanche-to-streamer transition. Furthermore, the discharge operating frequency also influences the streamer formation, and so the memory effect is frequency dependent. In light of all the factors that influence streamer formation, the value of S is best determined empirically from experimental data. We used experimental data from [26] to estimate the value of S for our system. For the simulation results presented here we used $S = 45$.

The main output from the program is a density map of the microdischarge activity in the simulated discharge volume that corresponds to the surface exposure of the photostimulable phosphor imaging plate or web. A typical result for a simulation over 20 discharge excitation cycles is shown in

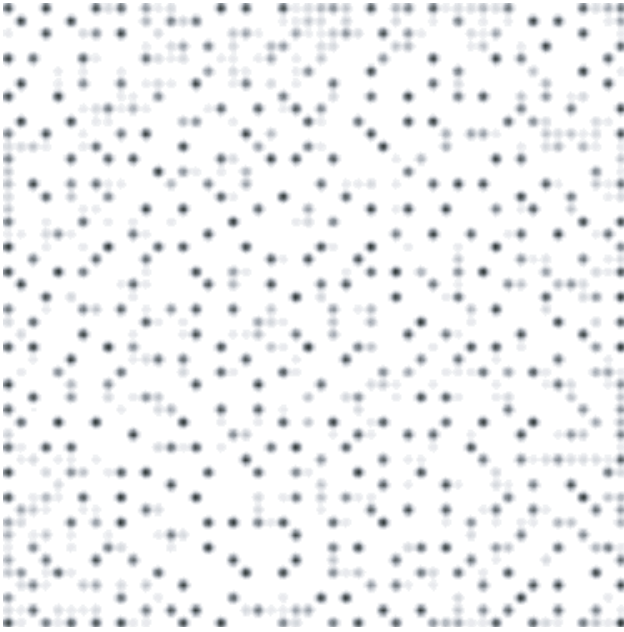


Figure 7. Simulation result on CA size 50×50 . This matrix represents the number of microdischarges recorded in CA. Total number of microdischarges recorded is 17 462.

figure 7. The DBD cell is driven by a 20.5 kHz sinusoidal voltage with a 4.5 kV amplitude, and the simulation was performed using a 50×50 lattice where the cell dimensions in the lattice are $1 \times 1 \times 0.762 \text{ mm}^3$. The grey scale intensity at any particular cell is proportional to the number of streamers striking the cell. The simulation shows that the occurrence of microdischarges across the simulation lattice is non-uniform: some regions are well treated by microdischarges and some are not treated at all. This non-uniformity is the result of interactions between microdischarges. Simulation results for image analysis were post-processed for better comparison with experimental images. The intensity of a microdischarge feature in a cell is given by the simulation, and the location of the microdischarge is assumed to be at the centre point of the cell. The size of each circular microdischarge feature is taken as the theoretically calculated diameter of the plasma channel. This information was used to construct a digital image with a pixel size equivalent to that in the experimental images. The results of post-processing are shown in figure 8. The post-processed digital images of the simulation results were further examined by image analysis and compared with image analysis of the experimental images. The post-processed simulation images show good qualitative agreement with the experimental storage phosphor images.

The present model is capable of simulating a complete DBD system for many excitation cycles. Previously reported models of DBDs were able to simulate only a small portion of a complete DBD system and only for a very limited time (usually tens of nanoseconds) [20, 30]. The present model is capable of not only simulating the working regime of a DBD system, but it also can simulate DBD starts. At the initiation of the discharge there are no microdischarge remnants capable of supporting the streamer formation at a low electric field. During the first period only a limited number of microdischarges will appear. When ‘preionization’ starts to accumulate in the discharge gap,

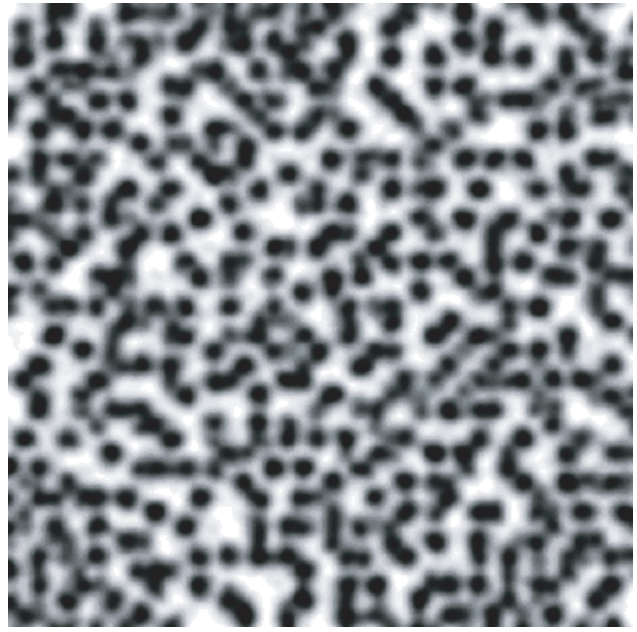


Figure 8. Simulation image of figure 7 (enlarged central portion of figure 7) with added noise for visual comparison with figure 2.

the number of microdischarges per period will increase until it reaches saturation level. The time needed to reach saturation level in our model is equal to about 12 periods. This is shown in figure 9.

Our streamer model does not consider simultaneously developed streamers, but since the time step is an adjustable parameter in our model, the time between successive streamers could be very small. To validate this assumption we measured the time lag between streamers experimentally (figure 11). We found that the average time lag between streamers is of the order of 70 ns, which is much larger than the time step in the model. So the model has sufficient time resolution to simulate the DBD with our experimental conditions. We tried different values for the time step in the model and found that 1 ns is sufficient to represent the various observed time intervals between streamers. Accordingly, we set the value of the time step (dt in figure 6) to a value of 1 ns. Based on the average time between streamer strikes, which is the duration of the excitation cycle divided by the number of microdischarges (about 50 ns in our case), we conclude that the time resolution chosen in our model is sufficient to represent microdischarge formation in DBDs under the conditions mentioned above.

Despite the fact that the model is relatively simple, it can capture the physics of the discharge very well. For example, the simulation model allows us to count the total number of microdischarges occurring under a given set of conditions. Each microdischarge that occurs can be assigned an index number, indicating its order of appearance. Although the number of microdischarges can be readily found experimentally, we present these results as a demonstration of the capabilities of the model. In figure 10, the calculated time interval between subsequent streamers is plotted as a function of the index number for one quarter of a period (shaded area on voltage plot). The plot shows that as the applied sinusoidal voltage approaches its maximum value, the time interval between streamers increases. The physical

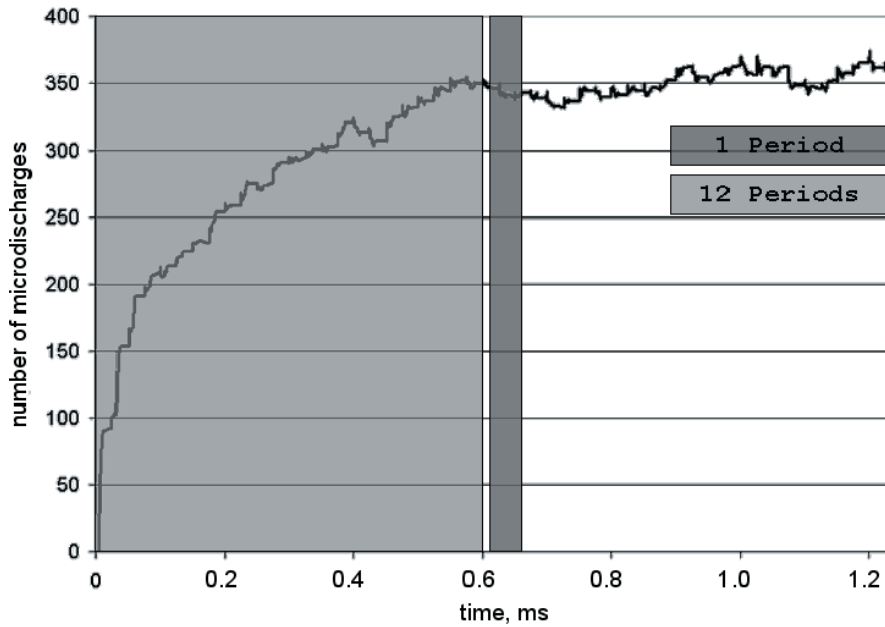


Figure 9. Simulation results showing the total number of microdischarges in the discharge gap with respect to time.

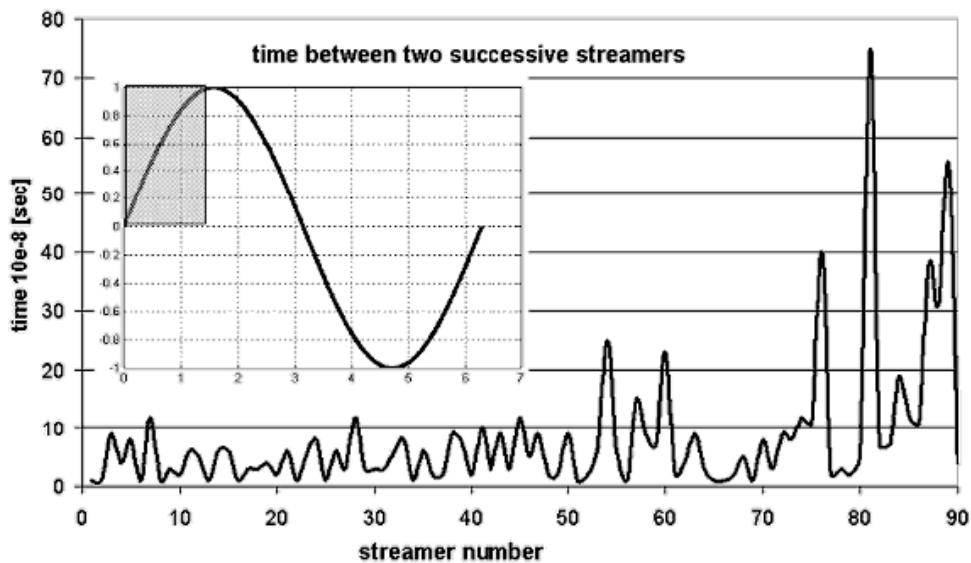


Figure 10. Simulation results showing the time interval between successive streamers (each streamer strike results in a microdischarge) during one quarter of a period (shaded area on the voltage plot).

meaning of this result is that, once a microdischarge occurs, the applied voltage must increase by some amount before another microdischarge can form. Therefore, the average time interval between successive streamers is related to the derivative of the voltage with respect to time.

By analysis of the optical pulse and secondary voltage waveforms from the experimental DBD cell, it is possible to determine the time interval between successive optical pulses resulting from either single or multiple microdischarges occurring in the field of view of the fibre optics mounted on the cell. Figure 11 shows the experimentally determined time interval between optical pulses from the discharge cell, when the discharge gap is 1.52 mm and the air flow is 1 slpm. The discharge area from which light was collected was 1.98 cm² (13.4 times smaller than the total discharge area). The data in

the figure 11 were accumulated over six half cycles and show that the average time interval between optical pulses is between 0.4 and 0.5 μ s. Thus the time lag for the total discharge area is about 30 ns. This is about 30 times greater than the time step in the simulation (1 ns).

7. Comparative analysis of experimental and simulated patterns

Our experimental results, as well as the theoretical results derived from our probabilistic models, are images with features that correspond to microdischarges. It is natural, then, to consider image analysis methods as a technique for making comparisons. Although there are many possible methods that

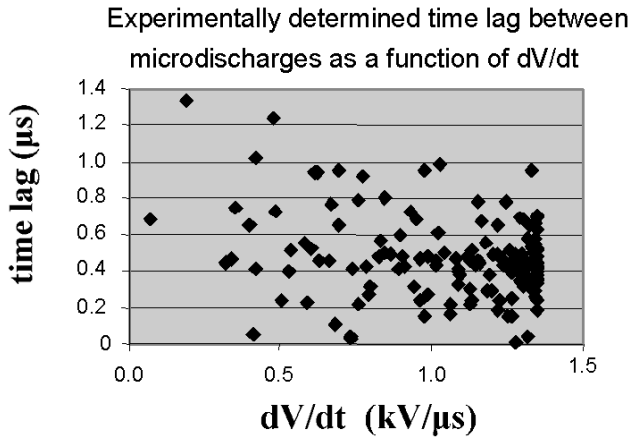


Figure 11. Experimentally determined time interval between optical pulses in a small part of the DBD discharge as a function of the voltage derivative.

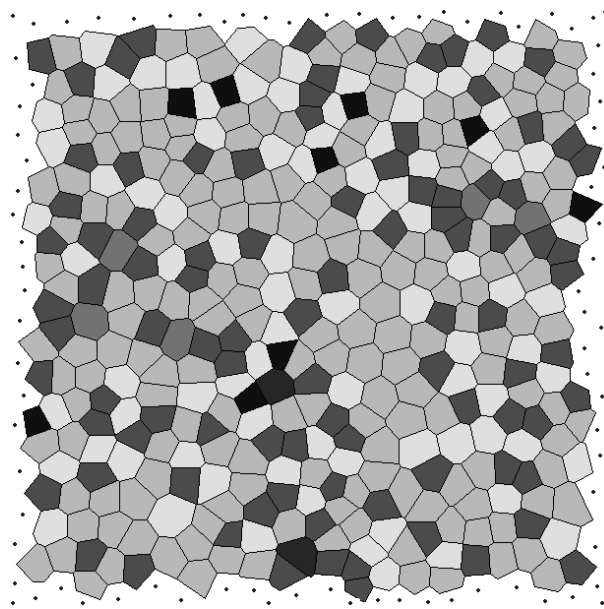


Figure 12. Voronoi polyhedra analysis of the experimentally obtained microdischarge locations from the image shown in figure 2. The polyhedra cells are grey scale coded according to the number of sides in each polyhedron. The cells in the image, obtained experimentally, are mainly six-sided cells and have similar sizes.

could be employed for this purpose, we focus here on the Voronoi polyhedron approach [24] and the two-dimensional correlation function [23] using random dot patterns as a baseline for comparison of the results. The random dot pattern simulates a streamer pattern in the absence of microdischarge interactions.

Voronoi polyhedra analysis defines polyhedral cells around selected features in an image, and the distribution of polyhedra types in the analysis can be used as a comparative tool. Voronoi polyhedra analysis is an excellent tool for measuring the homogeneity of patterns as well as for comparison of different patterns. The homogeneity can be easily estimated from the distributions of the Voronoi cell surface areas and used for comparison. Also, the topology of the pattern can be compared using the distribution of the number

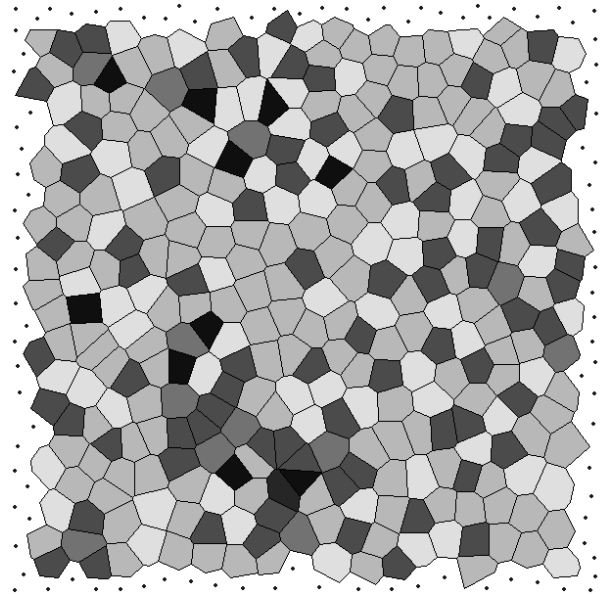


Figure 13. Voronoi polyhedra analysis of the simulated microdischarge locations from the image shown in figure 7. The polyhedra cells are grey scale coded according to the number of sides in each polyhedron. The cells in the image obtained in the simulation are mainly six-sided cells and have similar sizes.

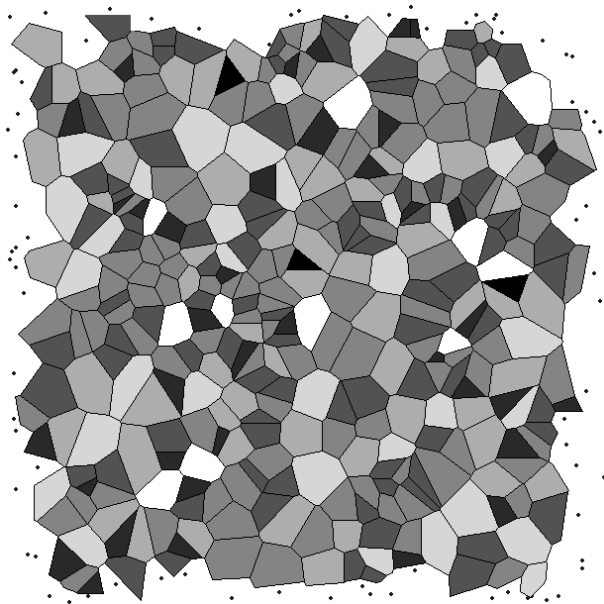


Figure 14. Voronoi polyhedra analysis of a random dot pattern for comparison with figures 12 and 13. The polyhedra cells are grey scale coded according to the number of sides in each polyhedron. The areas of different cells vary significantly.

of sides of Voronoi cells. This type of comparison is extremely useful in our case as it is invariant to stretching and rotation of the patterns, and also invariant to the particular positions of the microdischarge footprints. Although microdischarge patterns have never been analysed before using Voronoi polyhedra, this type of analysis is a standard for analysis of Coulomb crystals [23]. The Voronoi polyhedra analysis of an experimental image and its simulation is shown in figures 12 and 13, respectively. The Voronoi analysis of a random dot

pattern is shown in figure 14. A comparison of the Voronoi analysis of the random dot pattern with the simulated and experimental results shows that the random pattern is very different. This demonstrates the importance of short-range interaction between microdischarges in a DBD. One way of expressing numerically the difference between the images is to count the number of different-sided polyhedra determined in the Voronoi analysis. Unlike the random dot pattern, most of the polyhedral cells found in the analysis of the experimental and simulated images have six interior sides (six angles). This corresponds to the hexagonal lattice and thus implies radial symmetry of the interaction. This type of interaction was observed experimentally as well as predicted by our model. Although the model itself used a rectangular grid, the interaction symmetry is well preserved. Thus the cell size used in the model was small enough to resolve microdischarge interactions. Figure 15 shows the distribution of polyhedra

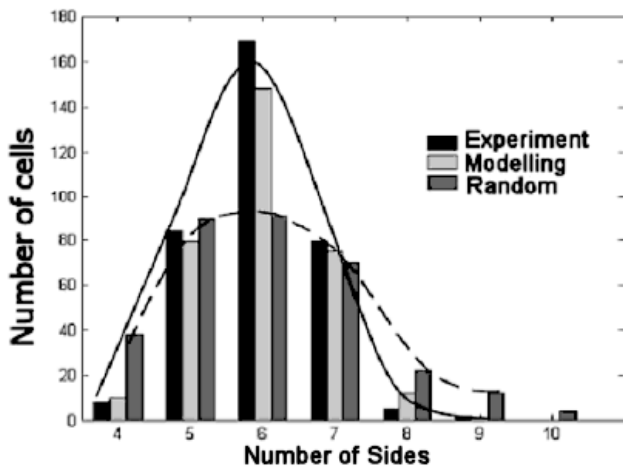


Figure 15. Distribution of Voronoi cell sides. The experimental data (figure 13), simulation data (figure 12) and data from a random-point distribution are shown for comparison.

types in the Voronoi analysis. The different polyhedra types in figure 15 are designated by the number of interior sides in a given polyhedral cell from the Voronoi analysis. The random dot pattern shows a markedly different distribution of polyhedra types when compared with the experimental and simulated images. This means that in our experimental and theoretical conditions interaction between microdischarges appears to have a strong effect.

The correlation function is widely used for post-processing in crystallography and can provide some indication of the correlation between features in a data set. The correlation function of the experimental image and the simulation are shown in figure 16 with open and solid signs, respectively. The correlation function for random dots is shown in figure 16 with the line without signs. As is expected for a random distribution of dots on a plane, it does not show any periodic oscillations in the correlation function. The correlation function for a completely ordered lattice should show strong oscillations or peaks, indicating that all the features in the image are related by well-defined unit cell vectors. As the spatial correlation between features in the image decreases, the peaks in the correlation function dampen. For example, the correlation function for a two-dimensional liquid with short-range correlation will look similar to the experimental and modelling curve in figure 16, where a strong oscillation shows up at short distances and then dampens out as a result of disorder. The overall agreement of the correlation function plots for the experimental and simulated images demonstrates that the features observed in the experimental image are not arranged randomly but are strongly influenced by microdischarge interactions in the DBD.

8. Concluding remarks

The two-dimensional spatial distribution of microdischarges in atmospheric pressure DBDs in air was studied both experimentally and theoretically. It was found that, under

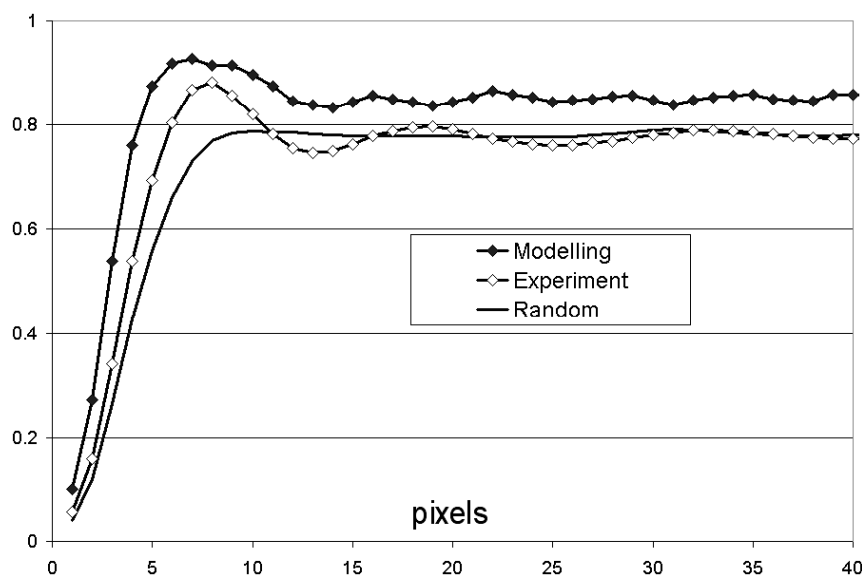


Figure 16. Two-dimensional correlation functions of (—◇—) experimental image from figure 2; (—◆—) simulation data from figure 7; and (—) data form a random-point distribution (shown for comparison).

certain conditions, streamers in a DBD do not strike randomly and the microdischarges they form interact and arrange themselves into a regular filament pattern. A new technique for obtaining Lichtenberg figures of DBDs in air using photostimulable (storage) phosphors is described. The discharge images obtained suggest that short-range interactions between microdischarges are present in the discharge.

We developed a microdischarge interaction model based on the assumption that the avalanche-to-streamer transition and thus microdischarge formation is influenced by microdischarge remnants. The model is capable of simulation of a complete DBD system for many excitation cycles. Previously reported models of DBDs were able to simulate only a small portion of a complete DBD system and only for a very limited time (usually tens of nanoseconds). The simulation results show qualitative agreement with experimental results and demonstrate the importance of the microdischarge interaction in barrier discharges. Short-range interaction between microdischarges and the resulting filament pattern can be predicted using the developed model of interaction.

Also, a new method for analysis of microdischarge patterns is proposed based on Voronoi polyhedra, which is invariant to the position of particular microdischarges, arbitrary stretching and rotation of the pattern. Using this method, the results of the simulation were compared with the experimental results, yielding convincing evidence of microdischarge interactions in DBDs, and demonstrating the validity of the model [32].

References

- [1] Hood J L 1980 *Int. Conf. on Gas Discharges and their Applications (Edinburgh)* pp 86–90
- [2] Uehara T 1999 *Adhesion Promotion Techniques* ed K L Mittal and A Pizzi (New York: Dekker) pp 139–74
- [3] Kogelschatz U 2002 *IEEE Trans. Plasma Sci.* **30** 1400–8
- [4] Falkenstein Z and Coogan J J 1997 *J. Phys. D: Appl. Phys.* **30** 817–25
- [5] Rosenthal L A and Davis D A 1975 *IEEE Trans. Indust. Appl.* **1a-11** 328–35
- [6] Lofthus A and Krupenie P H 1977 *J. Phys. Chem. Ref.* 113–307
- [7] Eliasson B and Kogelschatz U 1991 *IEEE Trans. Plasma Sci.* **19** 309–23
- [8] Lichtenberg G C 1777 *Novi. Comment. Gott.* **8** 168
- [9] Merrill F H and Von Hippel A 1939 *J. Appl. Phys.* **10** 873–87
- [10] Anemiya Y 1995 *J. Synchrotron Radiat.* **2** 13–21
- [11] Takahashi K, Tazaki S, Neriishi K and Etoh M 1998 *Fujifilm Res. Dev.* **43** 41–6
- [12] Ben-Kish A, Fisher A, Cheifetz E and Schwob J L 2000 *Rev. Sci. Instrum.* **71** 2651–4
- [13] Johnston R F, Pickett S C and Barker D L 1990 *Electrophoresis* **11** 355–60
- [14] Matsuda K, Kijima T, Atsumi H, Tsuji Y and Hatado M 1991 *RadTech Asia '91: Conf. Proc.* (Northbrook, IL: RadTech Int. North A.) pp 540–4
- [15] Keller D S and Pawlak J J 2001 *J. Pulp Paper Sci.* **27** 117–23
- [16] Kogelschatz U, Eliasson B and Egli W 1997 *J. Phys. IV 7 (Colloque C4, October 1997)* C4-47–66
- [17] Mikhailin V V and Terekhin M A 1989 *Nucl. Instrum. Methods Phys. Res. A* **282** 607–9
- [18] Thoms M and von Seggern H 1994 *J. Appl. Phys.* **75** 4658–61
- [19] Radzhabov E and Kurobori T 2001 *J. Phys.: Condens. Matter* **13** 1159–69
- [20] Gonzalez A L, Li H, Mitch M, Tolk N and Duggan D M 2002 *Appl. Radiat. Isotopes* **57** 875–82
- [21] Kurvich A M, Mikhailin V V, Myagkova M G and Terekhin M A 1990 *Vestnik, Moskovskogo Univ., Seriya 3, Fiz., Astrono.* **31** 44–8
- [22] Morrow R and Lowke J J 1997 *J. Phys. D: Appl. Phys.* **30** 614–27
- [23] Kulikovskiy A 1997 *IEEE Trans. Plasma Sci.* **25** 439–46
- [24] Steinle G, Neundorf D, Hiller W and Pietralla M 1999 *J. Phys. D: Appl. Phys.* **32** 1350–6
- [25] Liu S and Neiger M 2003 *J. Phys. D: Appl. Phys.* **36** 1565–72
- [26] Kupershtokh A L, Charalambakos V, Agoris D and Karpov D I 2001 *J. Phys. D: Appl. Phys.* **34** 936–46
- [27] Gutowitz H 1990 *Cellular Automata: Theory and Experiment* (Amsterdam: Elsevier, North-Holland)
- [28] Zuzic M, Ivlev A V, Goree J, Morfill G E, Thomas H M, Rothermel H, Konopka U, Sutterlin R and Goldbeck D D 2000 *Phys. Rev. Lett.* **85** 4064–7
- [29] Thomas H, Morfill G E, Demmel V, Goree J, Feuerbacher B and Mohlmann D 1994 *Phys. Rev. Lett.* **73** 652–5
- [30] Kogelschatz U 2001 Filamentary and diffuse barrier discharges *APP Spring Meeting, Bad Honnef, 18–21 February*
- [31] Aints M, Haljaste A, Kudu K and Plank T 1997 *J. Phys. D: Appl. Phys.* **30** 210–20
- [32] Babaeva N Y and Naidis G V 1996 *J. Phys. D: Appl. Phys.* **29** 2423–31
- [33] Meek J M 1940 *Phys. Rev.* **57** 722–8
- [34] Xu X P and Kushner M J 1998 Multiple microdischarge dynamics in dielectric barrier discharges *J. Appl. Phys.* **84** 8
- [35] Xu X P and Kushner M J 1998 Multiple microdischarge dynamics in dielectric barrier discharges *J. Appl. Phys.* **84** 4153–60
- [36] Braun D, Gibalov V I and Pietsch G J 1992 Two-dimensional modelling of the dielectric barrier discharge in air *Plasma Sources Sci. Technol.* **1** 166–74
- [37] Tsai P P, Wadsworth L C and Roth J R 1997 Surface modification of fabrics using one-atmosphere glow discharge plasma to improve fabric wettability *Textile Res. J.* **67** 359
- [38] Chirokov A, Gutsol A, Fridman A, Sieber K D, Grace J M and Robinson K S 2003 *ISPC-16 (Taormina, Italy, 22–27 June 2003)*